

Operando Detection of Lithium Plating and Stripping in Fast-Charging Li-Ion Cells with a Reference Electrode

Alexia Bichon, Sylvie Geniès, Philippe Azaïs, Didier Buzon, and Olivier Raccourt*

Understanding degradation mechanisms in Li-ion cells is essential for advancing fast-charging technologies. One of the primary limitations of fast charging is the risk of lithium plating, driven by the negative electrode potential. In this study, a reference electrode (RE) is integrated into 30 mAh pouch cells to investigate aging under various charging regimes. This three-electrode setup allowed monitoring the potential of both electrodes, with a particular focus on the negative electrode. By coupling operando data with post-mortem analysis, the cell's electrical behavior is linked to physical phenomena occurring within the cell. During fast charging at 2C, changes in the incremental capacity profile

are observed and correlated with a critical threshold in the negative electrode potential, measured using the RE. Post-mortem analysis confirmed that these changes are indicative of lithium plating. Furthermore, an additional current during the potentiostatic phase of the charge is identified, correlating with a rise in the potentials of both electrodes. This current bump is interpreted as evidence of a lithium stripping process. These findings highlight the importance of monitoring the negative electrode potential using an RE to detect and mitigate the risk of lithium plating during fast charging, contributing to the optimization of battery performance and safety.

1. Introduction

Lithium-ion batteries play a crucial role in the energy transition and the rise of electric vehicles (EVs).^[1] Their efficiency and reliability are essential for reducing our dependence on fossil fuels and promoting more sustainable modes of transportation. However, the complexity of these electrochemical systems requires a deep understanding and early detection of defects to ensure both performance and safety. The introduction of new materials in the Gen3b+ lithium-ion battery generation, such as silicon, has enabled an increase in the capacity of negative electrodes but has also introduced additional challenges, such as significant swelling during lithiation.^[2] This makes it particularly valuable to study these advanced battery technologies, as their aging mechanisms remain poorly understood.^[3–6] Among the aging mechanisms occurring within a lithium-ion battery, lithium plating and solid electrolyte interphase (SEI) growth are the

primary contributors to the consumption of active lithium ions. These side reactions collectively diminish the total capacity of the cell, leading to a noticeable decline in performance. In particular, lithium plating—a phenomenon where lithium ions are reduced and deposited in metallic form on the surface of the negative electrode—occurs under specific conditions, such as fast charging,^[7–9] and represents a major limitation for EVs general adoption. Preventing lithium plating is crucial, as it not only hinders fast-charging capabilities but also introduces severe safety hazards, including the potential for thermal runaway within the battery.^[10–13]

The use of a reference electrode (RE) inside a cell offers a substantial advantage, enabling the separate measurement of the potentials of the negative and positive electrodes. This capability provides crucial data for a detailed analysis of electrochemical phenomena, particularly for identifying the conditions that favor the onset of lithium plating on the negative electrode.^[14] Indeed, lithium plating may occur only when it is thermodynamically favorable, that is, when the electrochemical surface potential of graphite particles drops below 0 V versus Li⁺/Li.^[15] This condition can arise in several situations: during fast charging, which causes lithium-ion accumulation on the particle surfaces; at low temperatures, where ion diffusion within the solid is slowed; or at high state of charge (SOC) when the negative electrode becomes “saturated”.^[16] Lithium plating is a phenomenon that can develop locally within the cell, leading to heterogeneities in degradation.^[17–19] While the potential of the negative electrode, as measured with the RE, may serve as a reliable indicator of lithium plating formation, it cannot capture the local potential minima that may cause localized lithium plating.

The concept of RE has been previously explored using various designs and materials.^[20–25] REs make it possible to introduce a reference potential within the same electrochemical environment as the two other electrodes, allowing the individual measurement

A. Bichon, S. Geniès, D. Buzon, O. Raccourt

CEA, LITEN

DEHT

Univ. Grenoble Alpes
38000 Grenoble, France
E-mail: olivier.raccourt@cea.fr

P. Azaïs
CEA
DES
Univ. Grenoble Alpes
38000 Grenoble, France

 Supporting information for this article is available on the WWW under <https://doi.org/10.1002/batt.202500071>

 © 2025 The Author(s). *Batteries & Supercaps* published by Wiley-VCH GmbH. This is an open access article under the terms of the Creative Commons Attribution-NonCommercial-NoDerivs License, which permits use and distribution in any medium, provided the original work is properly cited, the use is non-commercial and no modifications or adaptations are made.

of the potential of either electrode. Liu et al.^[26] proposed the use of an RE within large cell formats to enable higher charging rates while maintaining the anode potential and temperature within safe operating limits. Similarly, Amietzajew et al.^[27] monitored the anode potential during the charging of a cylindrical cell at rates up to 2.2 C. Sieg et al.^[8] introduced a protocol incorporating a constant potential phase at the anode to mitigate the onset of lithium plating.

The detection of lithium plating onset has been explored by various methods. Adam et al.^[28] identified it using differential voltage analysis, correlating it to the anode potential. They observed an onset potential of ≈ -100 mV versus Li^+/Li , below the 0 V threshold at which lithium plating becomes thermodynamically feasible.^[29] Similarly, Chen et al.^[30,31] employed incremental capacity analysis (ICA) combined with post-mortem studies, identifying a peak at around 4 V, which they attributed to the onset of lithium plating.

Another approach to identifying the presence of lithium plating is to observe evidence of its reversibility. During lithiation, a fraction of the lithium plated on the graphite electrode can be reintercalated into the graphite host during subsequent delithiation, a process known as lithium stripping. This phenomenon has been modeled by von Lüders et al.^[32] and Hein et Latz^[33] and has been experimentally observed either during a relaxation phase following charging^[34] or at the beginning of the discharge step.^[35]

In this study, we combined operando data acquisition with post-mortem analysis of single-layer pouch cells to investigate the aging mechanisms on a $\text{LiNi}_{0.6}\text{Mn}_{0.2}\text{Co}_{0.2}\text{O}_2$ (NMC622) versus graphite (Gr) + 10% SiO_x battery cells. A significant amount of silicon was incorporated into the negative electrode to explore its impact on cell behavior. To gain insights into internal processes and degradation pathways, we introduced a “pseudo-reference” electrode based on lithium iron phosphate (LFP), selected for its optimal balance of stability, reliability, and durability under operando conditions. This pseudo-RE, referred to as RE throughout the rest of the paper, provides a sufficiently accurate measurement to confidently study potential variations and their impact on the cell’s behavior.^[36] Specifically, it enables the monitoring of the negative electrode potential to investigate the degradation phenomena.

Post-mortem analysis was conducted using scanning electron microscopy (SEM)² to visualize on the graphite electrode surface the lithium plating formed during charging rates ranging from C/3 to 2C. The incremental capacity curves were correlated with the anode potential measured simultaneously. This allows us to identify a specific lithium plating threshold on the anode potential. Lithium stripping was also investigated, revealing a distinct peak during the current decrease phase.

This research focuses on monitoring aging behavior under various operating conditions, with a specific aim to study the conditions that lead to lithium plating. Different constant current charging rates, from C/3 to 2C, were applied to evaluate their impact on plating formation during aging. Discharges were consistently performed at 1C. This approach allows for a clearer understanding of how charging regimes influence the onset and progression of lithium plating.

2. Experimental Section

The study utilized 30 mAh pouch cells with NMC-based positive electrode and Gr- SiO_x -based negative electrode, both made in laboratory. The positive electrode is composed of $\text{LiNi}_{0.6}\text{Mn}_{0.2}\text{Co}_{0.2}\text{O}_2$ (NMC622) from Targray, PVDF, Super P® (Imerys), and vapor grown carbon fiber, with a loading of 96% active material and $17.5 \pm 0.5 \text{ mg.cm}^{-2}$. Its porosity is $37 \pm 3\%$. The negative electrode is composed of graphite from Imerys with 10 wt% SiO_x from Shin Etsu, sodium carboxymethyl cellulose, styrene-butadiene rubber, and Super P® (Imerys), with a loading of 93.5% of active material and $7.7 \pm 0.4 \text{ mg.cm}^{-2}$. Its porosity is $30 \pm 3\%$. The electrolyte used is composed of ethylene carbonate to diethyl carbonate (1:1 v/v), 1 M LiPF_6 , +2 vol% vinyl carbonate, and 10 vol% fluoroethylene carbonate. The separator is composed of polypropylene (PP), 25 μm thin, with 41% porosity. The electrolyte was introduced in the cells with large excess. The electrodes are square-shaped with dimensions of 1225 mm^2 for the negative electrode and 1024 mm^2 for the positive electrode. The cells had a nominal capacity of 28 mAh, and the voltage range was set between 2.5 and 4.2 V.

The cells were equipped with an RE introduced on the negative electrode side of the separator and isolated from the electrode by an additional piece of separator (Figure 1). Typical result measuring over a charge and discharge cycle is given on Figure S2, Supporting Information. The design and size of the RE were carefully optimized to minimize disruption to the normal operation of the cell. The RE used is described in Chaouachi’s article,^[36] using aluminum mesh coated with LiFePO₄ (LFP) material as a pseudo-reference. The coated section of the RE is inserted a few millimeters between the cell layers, and represents a surface area of ≈ 10 to 15 mm^2 . The piece of separator, separating it from the negative electrode, is roughly twice as large, ensuring proper insulation. The RE is prefunctionalized before use, meaning that the LFP is delithiated to position it at its potential plateau of 3.424 V versus Li^+/Li .

A formation cycle of the cell, detailed in the supplementary information (see Figure S1, Supporting Information), is performed

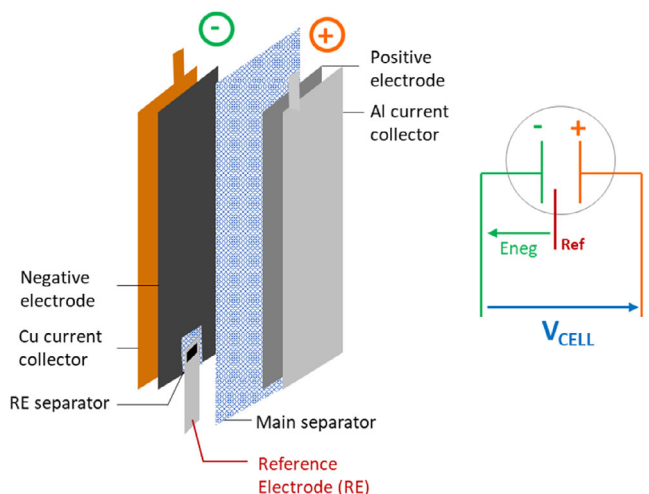


Figure 1. Schematic of a single-layer cell equipped with an RE and electrical measurement diagram.

at 45 °C prior to any use of the cell. The tests were done in a thermoregulated room maintained at 22 °C. Measurement of difference of potentials is done between RE and negative electrode, while the positive electrode potential is calculated by difference with cell voltage (Figure 1).

The cycling tests were conducted using BioLogic power supply (VMP3, ± 5 V, 400 mA max). A constant current constant voltage (CCCV) (until $I < C/10$) protocol was applied for charging, while discharging followed a constant current (CC) protocol. For the aging tests, various C-rates were applied during the charging phase: C/3, C/2, 1C, and 2C, with all discharge phases performed at a fixed rate of 1C. All the discharge steps of the aging were done at 1C. An initial checkup (CU_0) was carried out at C/10 ($I = 2.8$ mA), in a controlled room temperature (22 °C) to determine the initial discharge capacity of the cells (Q_0). At least two cells were tested for each C-rate condition. A checkup, conducted under the same conditions as CU_0 , was performed at semi-regular intervals, with the frequency adjusted based on the aging degradation and the samples. Equivalent full cycles (EFC) were calculated to compare aging across different C-rates using the following expression

$$EFC = \frac{\sum_i \text{Discharge capacity of cycle } i}{\text{Discharge capacity of } CU_0} \quad (1)$$

The state of health (SOH) was determined as the ratio of the capacity measured during the intermediate characterization (CU_i) to the initial checkup (CU_0).

ICA was calculated by taking the derivative of the capacity (dQ) with respect to the voltage (dV). To smooth the resulting curve, a Savitzky–Golay filter was applied with the following parameters: window size was comprised between 11 and 21, polynomial order of 3. These parameters were chosen to balance noise reduction and the preservation of key features in the ICA curve.

Post-mortem analysis was conducted by opening the cells at 0% SOC (2.5 V) in an argon-filled glovebox with O₂ and H₂O levels maintained at ≤ 0.1 ppm. First, the electrodes and the separator were visually examined and photographed inside the glovebox to document their surface condition. Second, small pieces of the negative electrodes were carefully sampled and rinsed with

dimethyl carbonate (DMC, CAS 616-38-6). The samples were then transported in an air-tight transfer case to prevent exposure to air during transfer for SEM (Zeiss) observations.

3. Results and Discussion

3.1. Cell Aging

The results of the aging test are presented in Figure 2, comparing the aging progression at different charging C-rates based on EFC to compare the different cells. After 100 cycles, the two cells charged at a C/3 rate exhibited a SOH between 80 and 85%, while those charged at a C/2 rate showed an SOH between 75 and 82%. We observe that the cells charged at lower C-rates (C/3 and C/2) exhibited similar aging profiles, with a very small difference in SOH evolution observed throughout the aging process. However, at higher C-rates (1C and 2C), after 60 cycles, the cells charged at 1C exhibited a SOH of $\approx 69\%$ after around 60 cycles, while those charged at 2C showed a significant decline, with SOH ranging between 52 and 47% after 60 EFC. A notable decrease in capacity was observed, along with greater dispersion in SOH as the C-rate increased.

3.2. Post-Mortem Analysis

Photos shown in Figure 3 reveal substantial lithium plating on the negative electrodes of cells charged at 1C and 2C. At 1C, the presence of the RE—or more precisely, the piece of separator protecting it—was found to locally alter the current distribution between electrodes. However, we estimate that the measured potential remains unaffected, as the region surrounding the RE appears to be similarly covered with lithium plating as the rest of the electrode. Moreover, we included in the Supplementary Data, in Figure S3, Supporting Information, the aging results of four additional cells cycled under the same conditions as the 1C and 2C-aged cells, but without an RE. We observe that the cell without an RE exhibits an aging behavior equivalent to that of the instrumented cells, as its capacity fade lies within the dispersion range of the cells equipped with an RE. This indicates that, in our case, the presence of the RE does not have a major impact on the global aging behavior of the cells.^[37] We focused our observation on the center of the samples. We can see the lithium plating is more important for sample aged at 1C and 2C. These observations correspond to SOH values of 68% and 46%, respectively. The SEM images of the samples, available in the supplementary information (Figure S4, Supporting Information), confirm the presence of lithium plating on their surface. In contrast, the negative electrodes from the fresh cell and cells aged at C/3 and C/2, which retained an SOH of 80%, did not exhibit visible lithium plating. During the disassembly process, it was observed that lithium plating remained adhered to the separator surface in the cell aged at 2C. SEM observations were conducted on areas where the plating had not detached (see Figure S5, Supporting Information). The results show a correlation between the lithium plating and the C-rate charges. Cells charged at higher C-rates

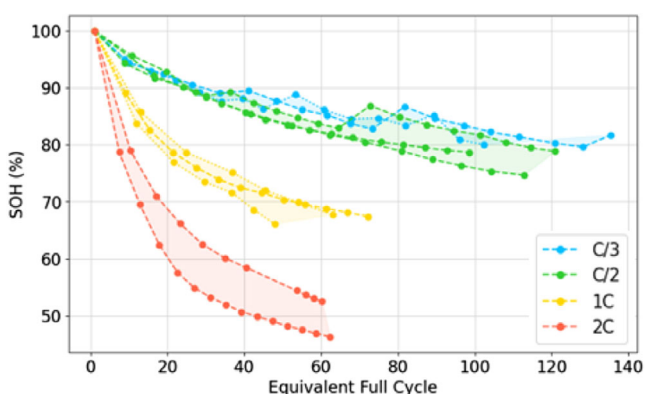


Figure 2. Evolution of the SOH of cells aged under different charging rates at room temperature.

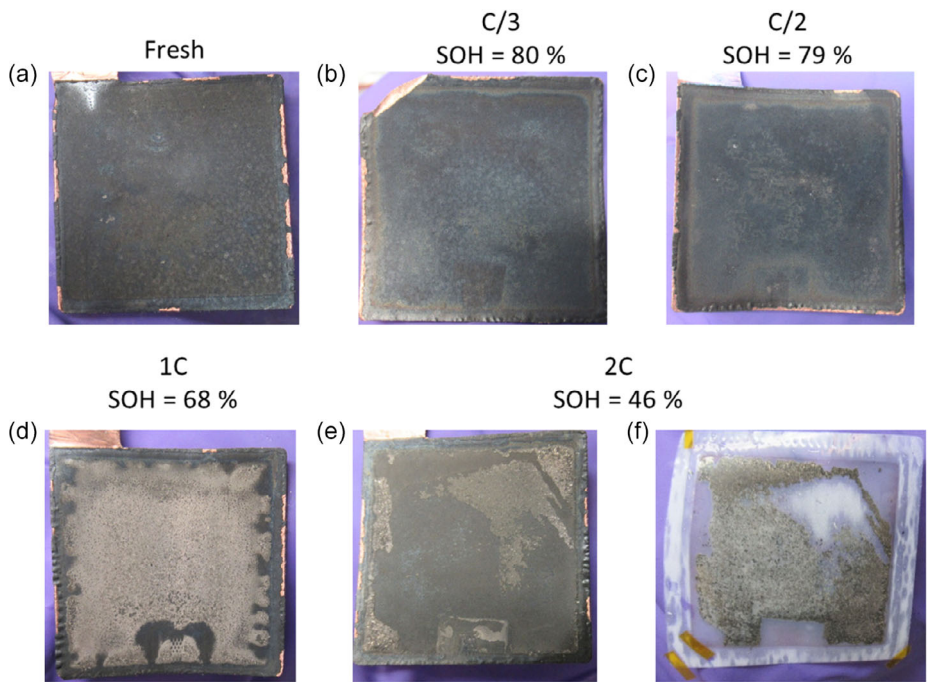


Figure 3. Photos of post-mortem analysis of negative electrodes at initial state a) and aged under different charging rates and stopped at various SOH: C/3 SOH = 80% b), C/2 SOH = 79% c), 1C SOH = 68% d), 2C SOH = 46% e). For the 2C cycling test with SOH = 46%, the separator covered partially by lithium plating detached from the negative electrode is shown f).

(1C and 2C) are more prone to significant lithium plating, which correlates with a notable decline in SOH. Conversely, cells charged at lower C-rates (C/3 and C/2) did not show such phenomena and maintained higher SOH values.

3.3. Aging Diagnosis

To gain insights into the degradation history of the cells, we analyzed RE data, focusing on the evolution of ICA profiles during charging at various C-rates. Figure 4 presents the evolution of the cell voltage and the negative electrode potential at C-rates of C/10, C/2, 1C, and 2C during the first charge cycle. The ICA curves of the cell voltage for each C-rate are also plotted in Figure 4a. The ICA profiles revealed distinct patterns that varied with the charging rate, shifting progressively towards higher voltages due to electrode polarization. Notably, a specific peak emerged at higher C-rates (1C and 2C), highlighted with bold lines on both graphs (a) and (b). This distinct moment in the charge cycle was correlated with the negative electrode potential data obtained via the RE. We observed that this peak corresponds to a region where the potential of the negative electrode drops significantly below 0 V versus Li⁺/Li. Additionally, the peak aligns with the same range of cell voltage and negative electrode potential. Based on these observations and consistent with the literature, we attribute this peak to the onset of lithium plating.^[30,38]

Following this analysis, we focused on the behavior of the negative electrode during charging at 2C over 9 successive cycles, with discharging conducted at 1C. Figure 5 presents four graphs

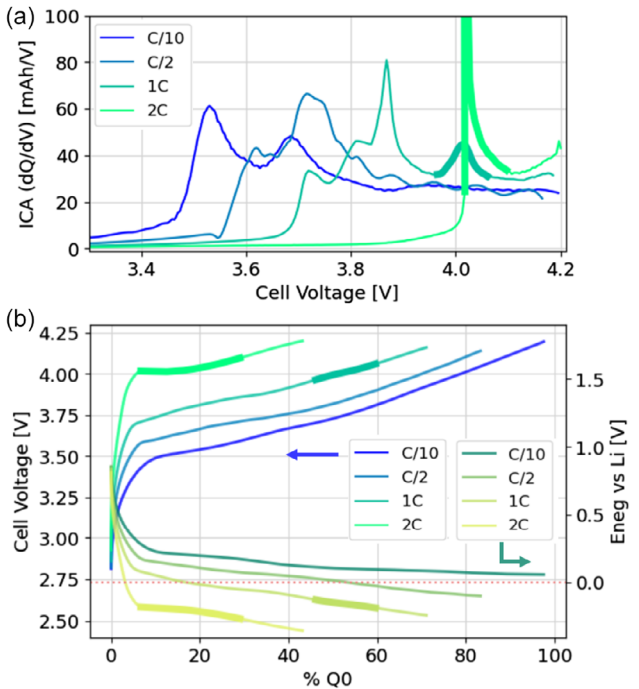


Figure 4. ICA a) and voltage b) profiles of a cell charged at various rates (C/10, C/2, 1C, 2C) at room temperature (RT). The peak corresponding to the onset of lithium plating is highlighted in bold on graph (a). On graph (b), the potential of the negative electrode is also included, with the corresponding voltage and negative electrode potential similarly highlighted in bold. The x-axis of graph (b) is expressed in terms of initial capacity (100% = initial cell capacity @ C/10).

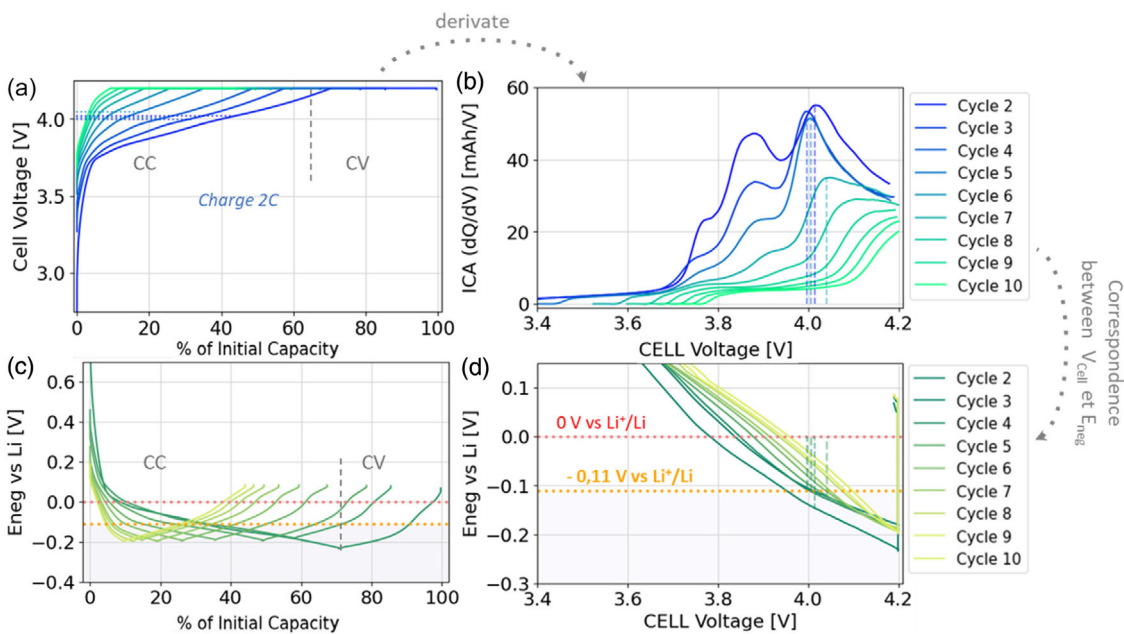


Figure 5. Correlation between cell voltage and negative electrode potential during the occurrence of the peak at 4 V on the ICA, indicating lithium plating within the cell. a) Cell voltage during 9 successive CCCV charges at 2C at RT (discharge at 1C). b) Corresponding ICA curves. c) Corresponding negative electrode potential curves measured by the RE. d) Correlation between cell voltage and negative electrode potential, enabling the determination of the negative electrode potential value associated with the summit of the peak on the ICA curve.

to support the subsequent analysis. Figure 5a shows the cell voltage during the CCCV charge at 2C for these 9 cycles. The associated ICA curves are displayed in Figure 5b, while the corresponding negative electrode potential is shown in Figure 5c. It is important to note that cycle 1, not showed on the graph, corresponds to the initial checkup cycle conducted at C/10, concluded with a complete discharge at 2.5 V. Consequently, the first 2C charge covers the entire SOC range. However, subsequent discharges at 1C are only partial due to polarization effects, which cause the cell to reach 2.5 V before complete delithiation. In Figure 5b, the previously observed peak at around 4 V is particularly noticeable during the first four cycles. The cell voltage values corresponding to these peaks maxima are recorded in Table 1. By plotting the cell voltage values against the negative electrode potential in Figure 5d, we were able to correlate the cell voltage peaks with the negative electrode potential measured by the RE at the time they occurred. Table 1 also includes the negative electrode potentials corresponding to the peak appearances, which were consistently between -0.15 and -0.11 V versus Li^+/Li . Based on these observations, we established -0.11 V versus Li^+/Li as the critical potential threshold for lithium plating

under the specific cycling conditions of our study. This threshold enables the detection of lithium plating onset during charging in operando by directly monitoring the cell voltage. This provides a valuable tool for the real-time prevention of this degradation mechanism, offering insights into improving the operational safety and longevity of lithium-ion cells.

3.4. Lithium Stripping Detection

The phenomenon of lithium stripping was observed during charging at 2C in the CV phase at 4.2 V. Figure 6 breaks down the different steps of a CCCV charge at 2C on a fresh cell, showing the cell voltage, the negative electrode potential measured with the RE, and the current. First, the insertion of lithium ions into the negative electrode is observed until the potential of the RE reaches a plateau at -0.15 V versus Li^+/Li . Second, the lithium plating phase occurs during both the CC phase and the CV phase when the cell voltage reaches 4.2 V, and the current begins to decrease until it falls below C/10. During the CV phase, the negative electrode potential rises to a threshold of -0.10 V versus Li^+/Li . Third, at the end of the CV phase, the negative electrode potential continues to rise until it becomes positive. Simultaneously, the positive electrode potential (see Figure S6, Supporting Information) rises above 4.1 V. At this point, the current, which had been decreasing monotonically, shows an inversion in its slope, forming a bump in the curve. This change in slope indicates the appearance of a reverse current opposing the end-of-charge current. We attribute this phenomenon to the local reoxidation of lithium plating on the negative electrode, which cleared space for the incoming Li^+ ions from the positive electrode as it reached higher potential values. This process

Table 1. Correspondence between cell voltage, charge level, and negative electrode potential for the first four cycles where the peak on the ICA curves can be distinguished.

Cycles	Cell voltage [V]	State of charge [%Q0]	Eneg vs. Li^+/Li [V]
Cycle 2	4.02	43	-0.15
Cycle 3	4.00	32	-0.11
Cycle 4	4.01	24	-0.11
Cycle 5	4.05	17	-0.12

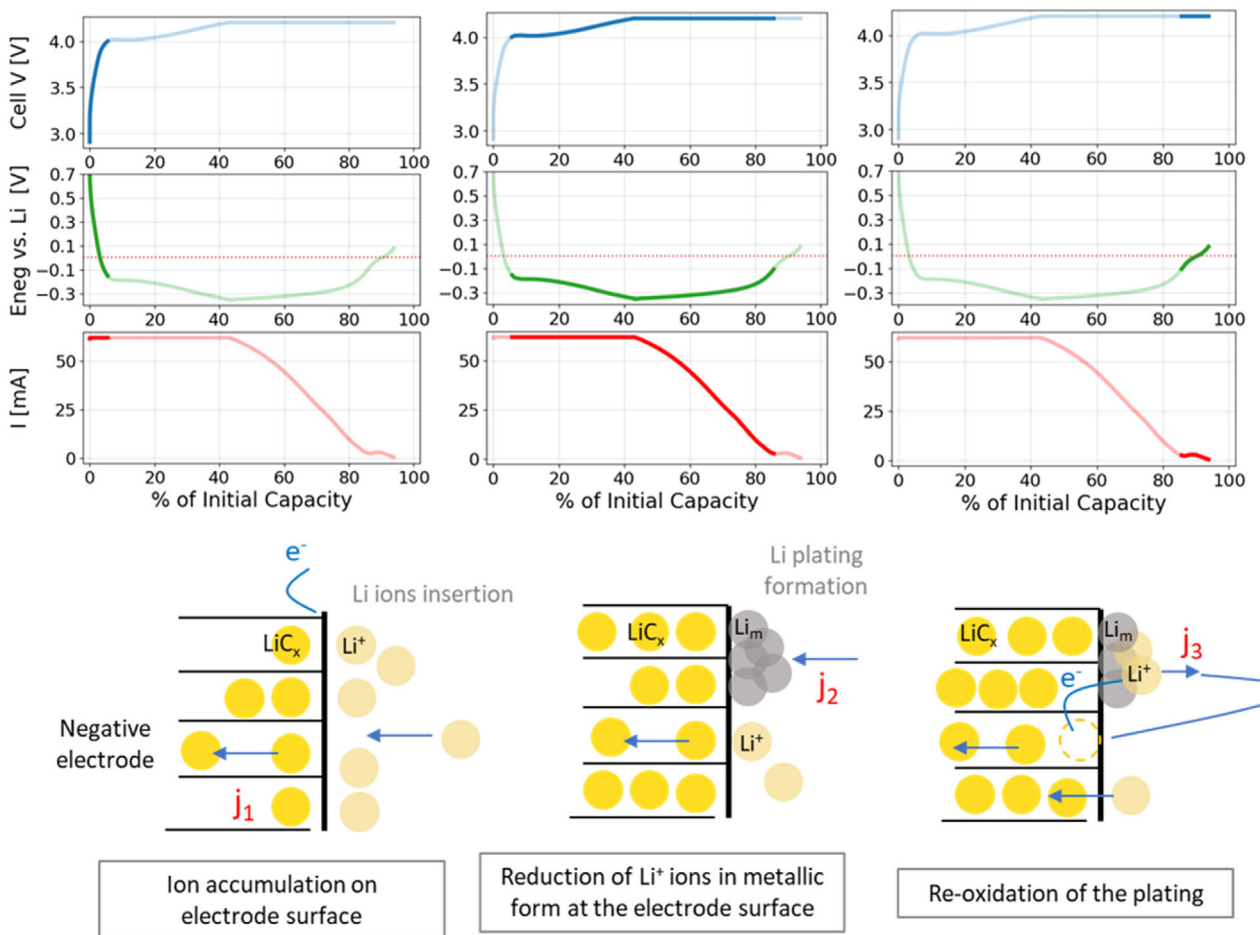


Figure 6. Proposed explanation of the successive phenomena encountered during cell charging: during the constant current phase, rapid voltage evolution occurs due to significant variation in the negative electrode potential corresponding to conventional Li-ion insertion (left). During the CCCV charging phase, the negative electrode potential drops below a threshold, leading to lithium plating formation (middle). Finally, at low current, partial reoxidation of the generated lithium plating is observed (right).

initiated a secondary lithiation phase at the end of the CV step, further contributing to the overall cell behavior during high C-rate charging.

We also recorded these current bumps during successive cycles. **Figure 7** presents cycles 2 to 9 under CCCV charging at 2C (with discharges at 1C, and cycles 1 and 10 corresponding to checkups). The figure highlights the current bump occurring at the end of the CV phase for each cycle, as well as the rise of the negative electrode potential beyond the threshold of -0.11 V versus Li^+/Li . This observation suggests that the current bump at the end of the CV phase, combined with the rise of the negative electrode potential above -0.11 V versus Li^+/Li , is a recurring phenomenon indicative of lithium stripping. These results are coherent to the previous observation in the literature.^[39,40]

Electrochemical impedance spectroscopy (EIS) was performed on the cycled cells at 1C with an RE at different SOH. Figure S7, Supporting Information, shows the EIS measurement of the full cell, the positive and the negative electrode on the fresh cell, at an intermediate aging stage ($\text{SOH} = 74\%$), and at a final aging stage ($\text{SOH} = 67\%$). This analysis was conducted on two cells cycled at 1C during both charge and discharge. The results obtained from the two cells were highly consistent,

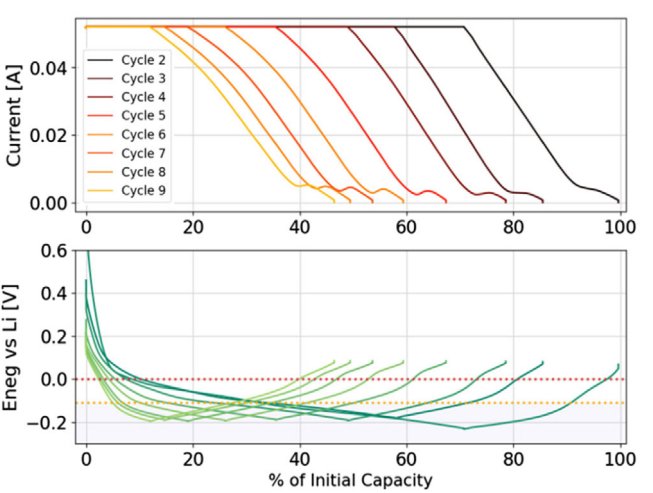


Figure 7. Current and negative electrode potential curves during successive CCCV charges at 2C, highlighting the coupling between the current bump and the electrode potential in each cycle.

demonstrating similar impedance trends across all SOH conditions. To interpret the EIS data, we used an equivalent electrical

circuit model composed of a series resistance R_0 , and two parallel RC elements: R_1C_1 and R_2C_2 , as shown in Figure S8, Supporting Information. In this model, R_0 corresponds to the ohmic resistance of the cell, mainly due to the electrolyte and current collectors. The R_1C_1 element is typically associated with charge transfer resistance and double-layer capacitance at the electrode/electrolyte interface, while R_2C_2 is often attributed to slower diffusion-related processes or interfacial phenomena (e.g., SEI growth or lithium plating). As the cell ages, all resistance components (R_0 , R_1 , R_2) tend to increase, reflecting the degradation of various components of the cell. However, for comparison purposes across SOH conditions, we chose not to distinguish individual contributions, but instead to focus on the total resistance ΔR , calculated as the sum of $R_0 + R_1 + R_2$ (Equation (2)). This global resistance metric captures the overall impedance evolution of the cell and allows a more straightforward analysis of aging effects.

$$\Delta R = \frac{R_0(t) + R_1(t) + R_2(t)}{R_0(t=0) + R_1(t=0) + R_2(t=0)} \times 100 \quad (2)$$

The results revealed a linear increase in resistance for the positive electrode and a marked step increase in the negative electrode resistance between intermediate and final stages. At 74% SOH, the rise in overall impedance was primarily due to the positive electrode. However, at 67% SOH, contributions from both electrodes significantly affected the total impedance. Notably, lithium plating was not detectable by EIS in the early aging phase but became evident at later stages as plating thickened and overall resistance increased.

These results show that, at an intermediate state of aging, the positive electrode contributes more significantly to the increase in resistance, while at an advanced state of aging, the negative electrode experiences a sudden increase in its impedance spectrum. This increase is correlated with the deposition of lithium plating on the surface of the negative electrode, which sharply raises the charge transfer resistance.

4. Conclusion

This study demonstrates the effectiveness of the RE as a valuable sensor for detecting and understanding lithium plating in lithium-ion cells, particularly under high C-rate cycling. The RE enabled precise monitoring of the negative electrode potential, allowing for the identification of critical conditions associated with lithium plating, which occurs around -0.11 V versus Li^+/Li in the context of this study. Our analysis revealed that little to no lithium plating was formed at lower C-rates (C/3 and C/2), while at higher C-rates (1C and 2C), aging was significantly accelerated with the formation of lithium plating. This was evidenced by characteristic changes in ICA profiles, and the appearance of current bumps during the CV phase of the charge, indicative of lithium stripping at the end of charging. The coupling of negative electrode potential curves with cell voltage profiles provided a deeper understanding of lithium plating and stripping processes, as well as their evolution over time. These findings underscore the

relevance of the RE as a practical tool for optimizing fast-charging protocols and minimizing high-rate degradation. By integrating this sensor into battery management systems, it could enhance the detection and prevention of critical conditions, such as lithium plating, ultimately improving battery longevity and safety in future applications.

Acknowledgements

The CEA Battery FOCUS program on "Multiscale simulation of batteries applied to electrode materials" is acknowledged for financial support. The authors would like to thank BATTERY2030+ large-scale initiative under H2020 European research program (grant agreement no. 957213) for the ecosystem and roadmap objectives in smart battery.

Conflict of Interest

The authors declare no conflicts of interest.

Author Contributions

Alexia Bichon: conceptualization (equal); data curation (lead); formal analysis (lead); investigation (lead); methodology (lead); visualization(lead); writing—original draft (lead); writing—review editing (equal). **Sylvie Geniès:** conceptualization (equal); data curation (supporting); formal analysis (equal); investigation (equal); methodology (equal); resources (equal); supervision (equal); validation (equal); visualization (supporting); writing—review editing (equal). **Philippe Azaïs:** conceptualization (equal); funding acquisition (equal); methodology (supporting); supervision (equal); validation (equal); writing—review editing (equal). **Didier Buzon:** conceptualization: supporting; supervision (equal); writing—review editing: supporting. **Olivier Raccut:** conceptualization (equal); funding acquisition (lead); methodology (equal); project administration (lead); supervision (lead); writing—review editing (equal).

Data Availability Statement

The data that support the findings of this study are available from the corresponding author upon reasonable request.

Keywords: cell aging • incremental capacity profiles • lithium plating • lithium-ion batteries • post-mortem • reference electrodes

- [1] P. Jaramillo, S. Kahn Ribeiro, P. Newman, S. Dhar, O.E. Diemuodeke, T. Kajino, D.S. Lee, S.B. Nugroho, X. Ou, A. Hammer Strømman, J. Whitehead, (Eds. P.R. Shukla, J. Skea, R. Slade, A. Al Khourdajie, R. van Diemen, D. McCollum, M. Pathak, S. Some, P. Vyas, R. Fradera, M. Belkacemi, A. Hasija, G. Lisboa, S. Luz, J. Malley), *In IPCC, 2022: Climate Change 2022: Mitigation of Climate Change*, Cambridge University Press, Cambridge, UK and New York, NY, USA 2022, <https://doi.org/10.1017/9781009157926.012>.

- [2] G. G. Eshetu, H. Zhang, X. Judez, H. Ade, nusi, M. Armand, S. Passerini, E. Figgemeier, *Nat. Commun.* **2021**, *12*, 5459.
- [3] S. Annegret, T. Hettesheimer, C. Neef, T. Schmaltz, S. Link, M. Stephan, J. L. Heizmann, A. Thielmann, *Fraunhofer Inst. Syst. Innov. Res. ISI* **2023**. <https://doi.org/10.24406/publica-1342>.
- [4] J. Vetter, P. Novak, M. R. Wagner, C. Veit, K.-C. Moller, J. O. Besenhard, M. Winter, M. Wohlfahrt-Mehrens, C. Vogler, A. Hammouche, *J. Power Sources* **2005**, *147*, 269.
- [5] R. Bednorz, T. Gewald, *Batteries* **2020**, *6*, 34.
- [6] S. Bazlen, P. Heugel, O. von Kessel, W. Commerell, J. Tübke, *J. Energy Storage* **2022**, *49*, 104044.
- [7] A. Adam, J. Wandt, E. Knobbe, G. Bauer, A. Kwade, *J. Electrochem. Soc.* **2020**, *167*, 130503.
- [8] J. Sieg, J. Bandlow, T. Mitsch, D. Dragicevic, T. Materna, B. Spier, H. Witzenhausen, M. Ecker, D. U. Sauer, *J. Power Sources* **2019**, *427*, 260.
- [9] A. Tomaszewska, Z. Chu, X. Feng, S. O'Kane, X. Liu, J. Chen, C. Ji, E. Endler, R. Li, L. Liu, Y. Li, S. Zheng, S. Vetterlein, M. Gao, J. Du, M. Parkes, M. Ouyang, M. Marinescu, G. Offer, B. Wu, *eTransportation* **2019**, *1*, 100011.
- [10] P. Kuntz, L. Lonardoni, S. Genies, O. Raccurt, P. Azaïs, *Batteries* **2023**, *9*, 427.
- [11] P. Münter, M. Diehl, J. E. Frerichs, M. Börner, M. R. Hansen, M. Winter, P. Niehoff, *J. Power Sources* **2021**, *484*, 229306.
- [12] B. Ng, P. T. Coman, E. Faegh, X. Peng, S. G. Karakalos, X. Jin, W. E. Mustain, R. E. White, *ACS Appl. Energy Mater.* **2020**, *3*, 3653.
- [13] M. Fleischhammer, T. Waldmann, G. Bisle, B.-I. Hogg, M. Wohlfahrt-Mehrens, *J. Power Sources* **2015**, *274*, 432.
- [14] Z. M. Konz, E. J. McShane, B. D. McCloskey, *ACS Energy Lett.* **2020**, *5*, 1750.
- [15] N. Legrand, B. Knosp, P. Desprez, F. Lapicque, *J. Power Sources* **2014**, *245*, 208.
- [16] T. Waldmann, B.-I. Hogg, M. Wohlfahrt-Mehrens, *J. Power Sources* **2018**, *384*, 107.
- [17] F. B. Spingler, W. Wittmann, J. Sturm, B. Rieger, A. Jossen, *J. Power Sources* **2018**, *393*, 152.
- [18] P. P. Paul, V. Thampy, C. Cao, H.-G. Steinrück, T. R. Tanim, A. R. Dunlop, E. J. Dufek, S. E. Trask, A. N. Jansen, M. F. Toney, J. Nelson Weker, *Energy Environ. Sci.* **2021**, *14*, 4979.
- [19] M. S. Hosen, P. Yadav, J. Van Mierlo, M. Berecibar, *Energies* **2023**, *16*, 1046.
- [20] S. J. An, J. Li, C. Daniel, S. Kalnaus, D. L. Wood III, *J. Electrochem. Soc.* **2017**, *164*, A1755.
- [21] S. Solchenbach, D. Pritzl, E. J. Y. Kong, J. Landesfeind, H. A. Gasteiger, *J. Electrochem. Soc.* **2016**, *163*, A2265.
- [22] J. Zhou, P. H. L. Notten, *J. Electrochem. Soc.* **2004**, *151*, A2173.
- [23] Y. Xiao, R. Xu, C. Yan, J.-Q. Huang, Q. Zhang, M. Ouyang, *Adv. Funct. Mater.* **2022**, *32*, 2108449.
- [24] R. Raccichini, M. Amores, G. Hinds, *Batteries* **2019**, *5*, 12.
- [25] R. Wang, W. Cui, F. Chu, F. Wu, *J. Energy Chem.* **2020**, *48*, 145.
- [26] J. Liu, Z. Chu, H. Li, D. Ren, Y. Zheng, L. Lu, X. Han, M. Ouyang, *Int. J. Energy Res.* **2021**, *45*, 7918.
- [27] T. Amietszajew, E. McTurk, J. Fleming, R. Bhagat, *Electrochim. Acta* **2018**, *263*, 346.
- [28] A. Adam, E. Knobbe, J. Wandt, A. Kwade, *J. Power Sources* **2021**, *495*, 229794.
- [29] M. W. Verbrugge, B. J. Koch, *J. Electroanal. Chem.* **1997**, *436*, 1.
- [30] Y. Chen, L. Torres-Castro, K.-H. Chen, D. Penley, J. Lamb, M. Karulkar, N. P. Dasgupta, *J. Power Sources* **2022**, *539*, 231601.
- [31] Y. Chen, K.-H. Chen, A. J. Sanchez, E. Kazyak, V. Goel, Y. Gorlin, J. Christensen, K. Thornton, N. P. Dasgupta, *J. Mater. Chem. A* **2021**, *9*, 23522.
- [32] C. von Luders, J. Keil, M. Weersberger, A. Jossen, *J. Power Sources* **2019**, *414*, 41.
- [33] S. Hein, T. Danner, A. Latz, *ACS Appl. Energy Mater.* **2020**, *3*, 8519.
- [34] X.-G. Yang, S. Ge, T. Liu, Y. Leng, C.-Y. Wang, *J. Power Sources* **2018**, *395*, 251.
- [35] W. Mei, L. Jiang, C. Liang, J. Sun, Q. Wang, *Energy Storage Mater.* **2021**, *41*, 209.
- [36] O. Chauuchi, J.-M. Réty, S. Génies, M. Chandesris, Y. Bultel, *Electrochimica Acta* **2021**, *366*, 137428.
- [37] S. Genies, A. Bichon, D. Buzon, P. Balfet, C. Debruyne, E. Villemain, M. Ranieri, C. Septet, R. Franchi, Y. Reynier, P. Azaïs, O. Raccurt, *ECS Meet. Abstr.* **2023**, MA2023-02, 165.
- [38] T. Gao, Y. Han, D. Fraggedakis, S. Das, T. Zhou, C.-N. Yeh, S. Xu, W. C. Chueh, J. Li, M. Z. Bazant, *Joule* **2021**, *5*, 393.
- [39] R. Chen, S. Miao, Y. Jia, X. Zhang, J. Peng, K. Zhang, F. Wu, J. Zhao, Z. Li, W. Cai, *J. Mater. Chem. A* **2024**, *12*, 33427.
- [40] S. P. Rangarajan, C. Fear, T. Adhikary, Y. Barsukov, G. Dadheeck, P. P. Mukherjee, *Cell Rep. Phys. Sci.* **2023**, *4*, 101740.

Manuscript received: January 31, 2025

Revised manuscript received: April 11, 2025

Version of record online: April 15, 2025